Stem Cell Reports
Article

OPEN ACCESS

Steps toward Maturation of Embryonic Stem Cell-Derived Cardiomyocytes by Defined Physical Signals

Nian Shen,[1,2] Anne Knopf,[1,2] Claas Westendorf,[1] Udo Kraushaar,[3] Julia Riedl,[1,2] Hannah Bauer,[2] Simone Pöschel,[2] Shannon Lee Layland,[1,2] Monika Holeiter,[1,2] Stefan Knolle,[1,3] Eva Brauchle,[1,2] Ali Nsair,[4,5] Svenja Hinderer,[1,2] and Katja Schenke-Layland[1,2,4,*]

[1]Department of Cell and Tissue Engineering, Fraunhofer Institute for Interfacial Engineering and Biotechnology IGB, Stuttgart 70569, Germany
[2]Department of Women's Health, Research Institute of Women's Health, University Hospital of the Eberhard Karls University Tübingen, Tübingen 72076, Germany
[3]Department of Cell Biology, Electrophysiology, Natural and Medical Sciences Institute, University of Tübingen, Reutlingen 72770, Germany
[4]Department of Medicine/Cardiology, Cardiovascular Research Laboratories (CVRL), David Geffen School of Medicine, University of California Los Angeles (UCLA), Los Angeles, CA 90095, USA
[5]Broad Stem Cell Research Center, David School of Medicine at UCLA, Los Angeles, CA 90095, USA
*Correspondence: katja.schenke-layland@med.uni-tuebingen.de
http://dx.doi.org/10.1016/j.stemcr.2017.04.021

SUMMARY

Cardiovascular disease remains a leading cause of mortality and morbidity worldwide. Embryonic stem cell-derived cardiomyocytes (ESC-CMs) may offer significant advances in creating in vitro cardiac tissues for disease modeling, drug testing, and elucidating developmental processes; however, the induction of ESCs to a more adult-like CM phenotype remains challenging. In this study, we developed a bioreactor system to employ pulsatile flow (1.48 mL/min), cyclic strain (5%), and extended culture time to improve the maturation of murine and human ESC-CMs. Dynamically-cultured ESC-CMs showed an increased expression of cardiac-associated proteins and genes, cardiac ion channel genes, as well as increased SERCA activity and a Raman fingerprint with the presence of maturation-associated peaks similar to primary CMs. We present a bioreactor platform that can serve as a foundation for the development of human-based cardiac in vitro models to verify drug candidates, and facilitates the study of cardiovascular development and disease.

INTRODUCTION

Pluripotent stem cells (PSCs) hold immense therapeutic potential (Passier et al., 2008; Masumoto et al., 2012). PSC-derived cardiomyocytes (PSC-CMs) may offer significant advances toward creating novel pre-clinical in vitro test systems for disease modeling, drug toxicity screening, and drug sensitivity identification (Braam et al., 2009; Ebert et al., 2012; Yang et al., 2014). A number of research groups have established methods for the differentiation of PSCs into CMs (Zhang et al., 2012; Lundy et al., 2013; Nunes et al., 2013); however, the PSC-CMs displayed an immature phenotype when compared with adult CMs with respect to sarcomere structure (Yang et al., 2008), calcium-handling properties (Li et al., 2013), and electrophysiology (Blazeski et al., 2012; Ribeiro et al., 2015). PSC-CMs that are not fully matured may reduce their usability for drug testing and disease modeling, particularly when the disease-causing mutation affects a gene that is not expressed until later in development or if the disease occurs postnatally (Braam et al., 2009; Passier et al., 2008).

Cytoskeletal and rhythmic contraction, and pulsatile laminar shear stress, are mechanical forces that have been suggested to play a crucial role in heart development and growth (Taber, 2001; Zhu et al., 2014; Andrés-Delgado and Mercader, 2016). Cytoskeletal contraction is involved in several morphogenetic processes in the embryo (Taber, 2001). Rhythmic contraction is the exposure of CMs to regular cyclic stretch (Zhu et al., 2014). The heart is exposed to blood flow during most heart developmental stages and throughout adult life (Andrés-Delgado and Mercader, 2016). Pulsatile laminar shear stress generated by blood flow in healthy hearts influences heart chamber formation and maturation, trabeculation, CM proliferation, and valvulogenesis (Andrés-Delgado and Mercader, 2016). Employing physical signals to mimic cardiogenesis in vitro is a potential strategy to achieve PSC-CM maturation. Several groups have developed methods to apply uniaxial stress to PSCs (Tulloch et al., 2011; Wan et al., 2011; Mihic et al., 2014). Although uniaxial stress can promote PSC-CM maturation, using stretch alone does not mimic in vivo physical signals that act on CMs within the heart (Guan et al., 2011). Carrier et al. (2002) demonstrated that perfusion flow leads to a continuous medium change and therefore increases the spatial uniformity of CMs by improving the control of oxygen, pH, nutrients, and metabolites in the cellular microenvironment; however, the impact of pulsatile flow on PSC-CM maturation, or a possible synergistic effect of the combination of pulsatile flow and cyclic strain has not been investigated.

In the present study, we designed and evaluated a bioreactor system to expose mouse embryonic stem cell (mESC)- and human ESC (hESCs)-derived cells to defined mechanical stimuli. We investigated the impact of pulsatile

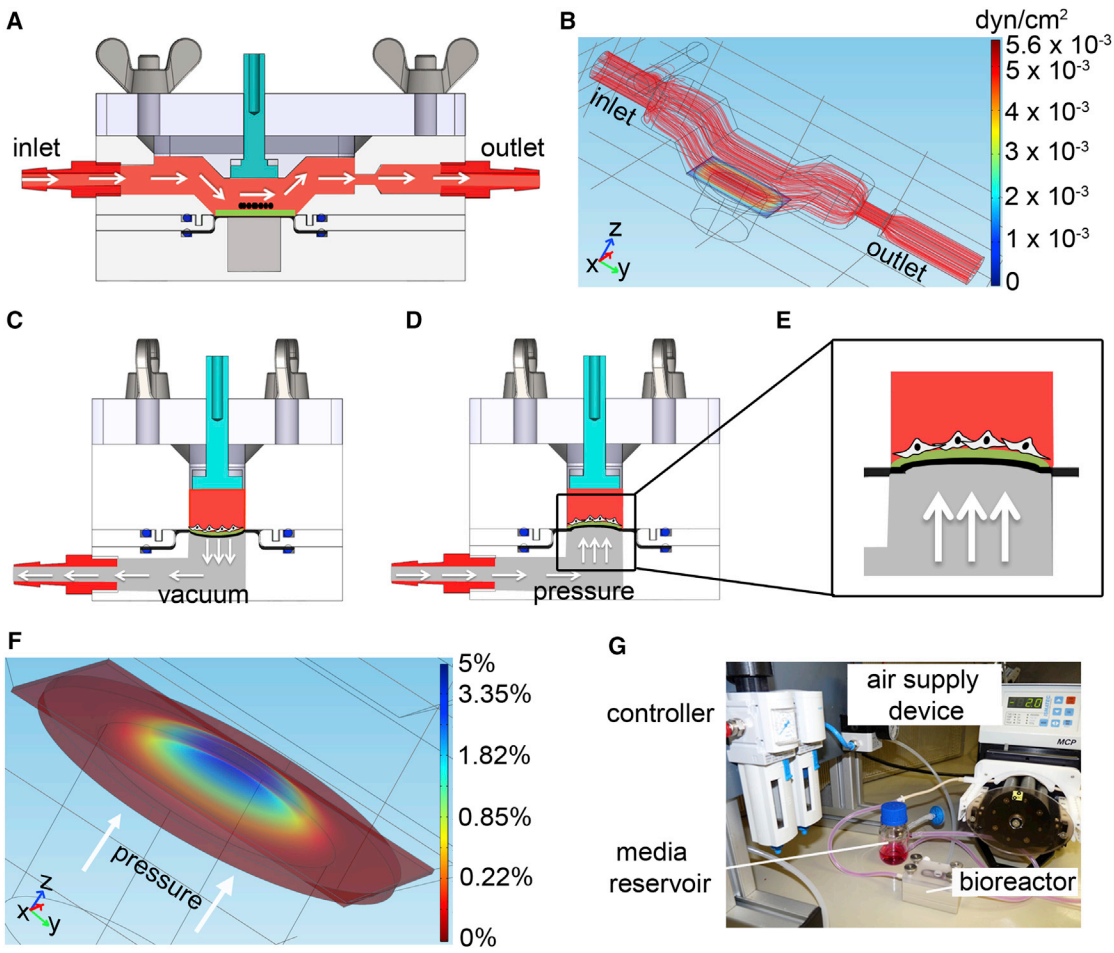

Figure 1. Bioreactor System Design and Evaluation

(A) Computer-aided design of the flow chamber (red) in a cross-sectional view. White arrows point in flow direction. Cell-seeded membrane in green. Silicone membrane is indicated in black.

(B) Representative simulation of wall shear stress distribution in the bioreactor system. Red stream lines indicate laminar flow.

(C–E) Vacuum- (C) and pressure-driven (D and E) mechanism to enable a physiological stretch profile. Pressure gradient is induced in the air chamber (gray) using a controller. White arrows show the direction of air. The cell-seeded membrane is depicted in green, and the silicone membrane is indicated in black.

(F) Representative strain distribution simulation of the cell-seeded membrane with 1.35 standard atmosphere pressure applied. White arrows show the direction of pressure.

(G) Photograph of the experimental setup. The bioreactor is coupled to a culture medium reservoir, an air supply device, and a controller.

flow-induced shear stress and physiological stretch on murine and human ESC-CM maturation in vitro by extensively analyzing cardiac protein and gene expression patterns. We analyzed the calcium-handling properties and sarcoendoplasmic reticulum Ca^{2+}-ATPase (SERCA) activity in dynamically-cultured CMs. In addition, we characterized the phenotype of ESC-CMs employing marker-free Raman microspectroscopy. Elucidating the effect of defined mechanical forces on the maturation of ESC-CMs is an essential step toward developing fully matured and functional cardiovascular tissues in vitro that can be used to study cardiovascular diseases and investigate potential drug candidates.

RESULTS

Bioreactor Design: In Silico and Functional Evaluation

A bioreactor system was designed and manufactured to induce a defined shear stress by exposing cells that were seeded on a membrane to laminar flow and a physiological strain. A computer-aided design (CAD) schematic of the bioreactor is displayed in Figures 1A and 1C–1E. Computer simulations were performed based on the geometry of the bioreactor using COMSOL. Simulations showed that a flow rate of 1.48 mL/min created a constant shear stress between 10^{-3} and 5.6×10^{-3} dyn/cm^2 over the entire

cell-seeded membrane (Figure 1B). Flow rates of 2.96 and 5.92 mL/min resulted in a shear stress ranging from 10^{-3} to 1.16×10^{-2} and 10^{-3} to 2.44×10^{-2} dyn/cm^2, respectively. A vacuum- (Figure 1C) and pressure- (Figures 1D and 1E) controlled air chamber generated a cyclic strain on the cell-seeded membrane that was placed on a silicone membrane, which separated the flow from the air chamber. Figure 1F illustrates the distribution of a gradient of strain (up to 5%) on the cell-seeded membrane created by a 1.35 standard atmosphere. Based on the simulation results, we seeded cells in the center of the membrane within a defined area to ensure a homogeneous stretching. The bioreactor system setup is illustrated in Figure 1G.

The Combination of a 1.48 mL/min Pulsatile Flow and 5% Cyclic Strain Increases Cardiac Gene and Protein Expression Patterns in mESC-Derived Cells after 12 Days in Culture

After confirming pluripotency of mESCs by immunofluorescence (IF) staining (Figure S1), cells were transferred to fibronectin-coated membranes for 1 day to allow cell attachment, before being exposed to static or dynamic culture conditions. To determine the appropriate mechanical stimuli required to induce cardiac differentiation and maturation, we subjected mESC-derived cells to an initial flow rate of 0.74 mL/min, and then increased the flow rates to 1.48, 2.96, or 5.92 mL/min from the second day until day 12, a time point that been described previously as appropriate to mimic early cardiogenesis (Davis et al., 2012). In parallel, we tested cyclic strains of 2.5%, 5%, or 10% at 0.33 Hz without flow for 12 days. Subsequently, cells were harvested for gene and protein expression analyses. The 1.48 mL/min flow rate led to significantly increased *Nkx2-5, Actc1, Myh6,* and *Myh7* gene expression and a higher number of sarcomeric myosin-positive (MF20$^+$) cells when compared with other flow conditions or static controls (Figures S2A–S2E and S2P). All strain conditions significantly increased the expression of cardiac-associated genes when compared with static controls (Figure S2F). No significant change in the number of MF20$^+$ cells was detected among the different strain settings (Figures S2G–S2J).

To investigate a possible synergistic effect of both pulsatile flow and cyclic strain, we exposed the mESC-derived cells to an initial flow rate of 0.74 mL/min, which was then increased to 1.48 mL/min on day 2 with simultaneous exposure to cyclic strain of 2.5%, 5%, or 10% (all at a frequency of 0.33 Hz). The combination of pulsatile flow and strain resulted in a significant increase in cardiac-associated gene expression when compared with the static controls (Figures S2K and S2P). MF20$^+$ cells cultured under flow and cyclic strain conditions displayed a more rod-like morphology (Figures S2L–S2N). The combination of 1.48 mL/min flow and 5% strain resulted in >20% increase in MF20$^+$ cells, which was the highest among all conditions and led to spontaneously beating clusters (Figure S2O). Therefore, further experiments were performed using a 1.48 mL/min pulsatile flow and 5% strain, to which we refer as the dynamic condition in the following paragraphs.

Combination of Prolonged Culture Time and Dynamic Conditions Results in Advanced Maturation of mESC-CMs

To verify whether exposure to prolonged dynamic conditions can further advance the maturation of mESC-CMs, we continuously cultured the cells for another 6 days (a total of 18 days in dynamic culture [d18 dyn mESC-CMs]). The d18 dyn mESC-CMs were then compared with day 12 dynamically-cultured cells (d12 dyn mESC-CMs) and static controls (d12 stat mESC-CMs and d18 stat mESC-CMs). d12 and d18 dyn mESC-CMs showed well-defined and aligned cross-striated sarcomeric structures as determined by the expression of MF20 and cTNT (Figure 2A). Randomly aligned fibers with no striated sarcomeric structures were seen in mESC-CMs cultured for either 12 or 18 days under static conditions (Figure 2A). Connexin 43 (CX43) IF staining of d18 dyn mESC-CMs indicated an increase in plasma membrane gap junctions when compared with the d12 stat and dyn mESC-CMs, and d18 stat mESC-CMs (Figure 2A). Sarcomere length was also increased in d18 dyn mESC-CMs when compared with d12 dyn mESC-CMs (Figure 2B). Sarcomeric structures were not detectable in either the d12 or d18 stat mESC-CMs (Figure 2B). cTNT expression in d18 stat and dyn mESC-CMs was examined using imaging flow cytometry to confirm the IF staining results. To ensure only viable cells were used for analysis, we excluded dead cells using Zombie Red dye (ZR). We observed a significant increase in the median fluorescence intensity (MFI) of cTNT in d18 dyn mESC-CMs when normalized to MFI of cTNT in d18 stat mESC-CMs (Figures 2C and 2D). In addition, a significant upregulation of cardiac-associated genes, including myosin heavy chain α (*Myh6*) and β (*Myh7*), cardiac myosin binding protein C (*Mybpc3*), troponin I1 (*Tnni1*), and troponin T2 (*Tnnt2*), was detected in d18 dyn mESC-CMs when compared with d18 stat mESC-CMs (normalized to *Gapdh* or *Rplp0*, Figure S3, Table S1).

Adult CMs express high levels of cardiac-specific ion channels, which contribute to the propagation of action potentials and contraction (Mihic et al., 2014). Therefore, we evaluated transcript levels of several cardiac ion channel genes in d18 stat and dyn mESC-CMs (Figure S3). A significant upregulation of the delayed-rectifier voltage-gated potassium hERG channel (*Kcnh2*; 6.3-fold normalized

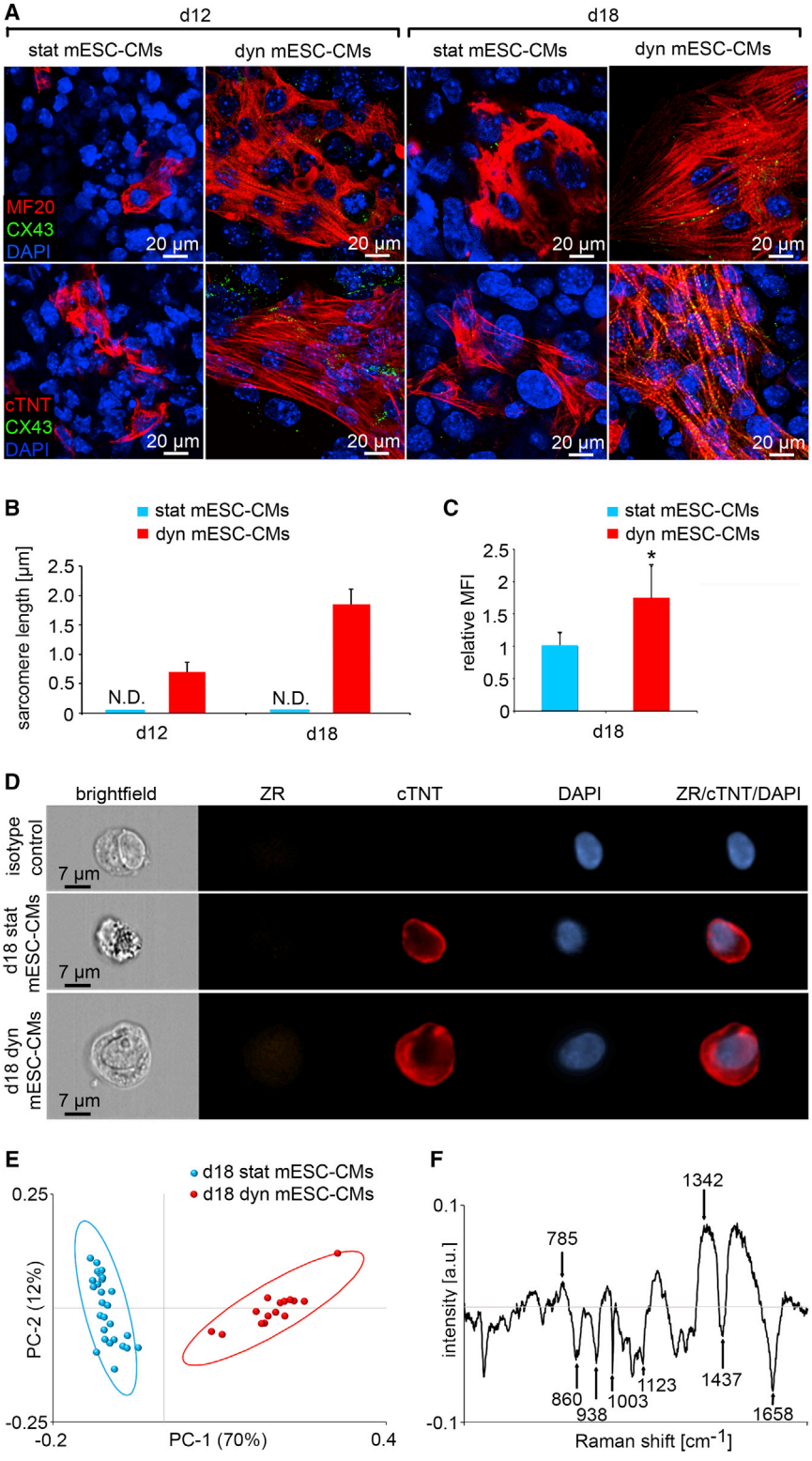

Figure 2. Mechanical Forces Enhance Cardiac Protein Expression Patterns in mESC-CMs

(A) IF staining of d12 stat and dyn, and d18 stat and dyn mESC-CMs using MF20 (red), CX43 (green), cTNT (red), and DAPI (blue).

(B) Sarcomere length in d12 and d18 mESC-CMs was quantified using ImageJ (n = 20 cells from three independent cultures each). Error bars show SD. N.D. = not detectable.

(C) Relative median fluorescence intensity (MFI) of cTNT expression in d18 stat mESC-CMs and d18 dyn mESC-CMs (n = 3). Error bars show SD. *p = 0.0490.

(D) Representative images of d18 stat mESC-CMs and d18 dyn mESC-CMs stained with ZR (orange), cTNT (red), and DAPI (blue) as well as the isotype control. ZR/cTNT/DAPI represents an overlay.

(E) Raman microspectroscopy results. Plotting of PC-1 and PC-2 score values depicts a distinction between d18 stat and d18 dyn mESC-CMs (n = 30 measurements from three independent cultures each). The ellipses mark the 95% confidence region for each sample.

(F) PC-1 loading describes the Raman shifts that vary in d18 dyn mESC-CMs when compared with d18 stat mESC-CMs. Differences between d18 stat and dyn mESC-CMs were identified at wavenumbers indicated by arrows (see also Figures S2 and S3).

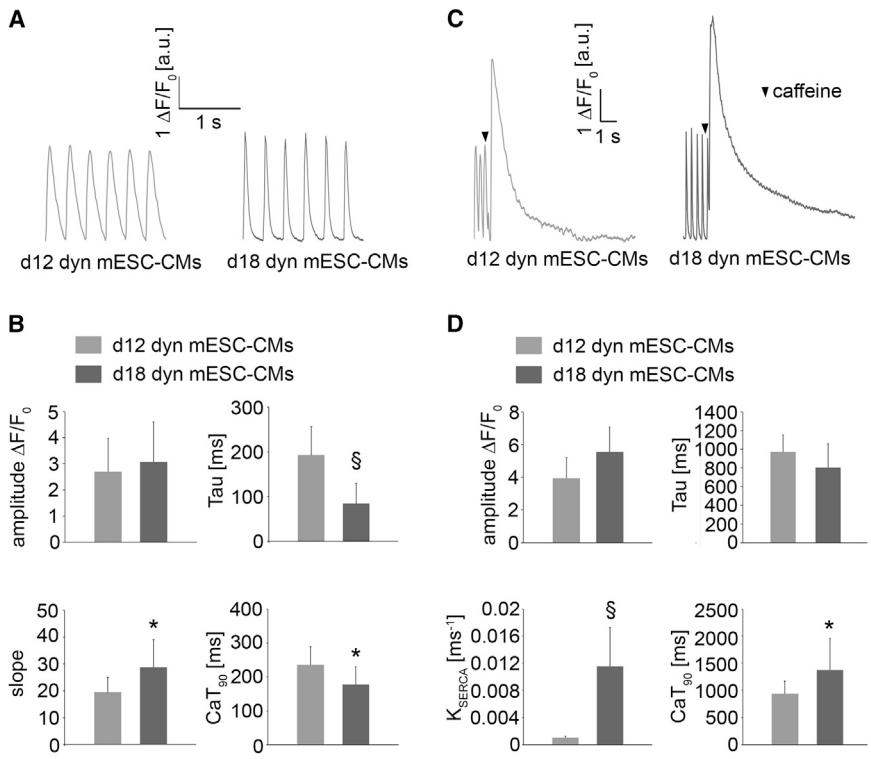

Figure 3. Calcium Transient Assessment of Dynamically-Cultured mESC-CMs

(A) Representative systolic Ca^{2+} transient traces recorded at the stimulation frequency of 3 Hz in d12 and d18 dyn mESC-CMs. Fluorescence intensities are displayed in a.u.

(B) Average amplitude, time constant of decay (tau), slope and Ca^{2+} transient duration (CaT_{90}) in d12 (n = 9) and d18 dyn (n = 11) mESC-CMs. Error bars show SD.

(C) Representative caffeine-induced changes in Ca^{2+} transient traces in d12 and d18 dyn mESC-CMs.

(D) Average caffeine-induced amplitude, time constant of decay (tau), SERCA activity, and Ca^{2+} transient duration (CaT_{90}) in d12 (n = 9) and d18 dyn (n = 11) mESC-CMs. Error bars show SD.

*$p < 0.05$, §$p < 0.001$.

to *Gapdh*; 4.6-fold normalized to *Rplp0*) and α1c subunit L-type calcium channel (*Cacna1c*; 3.6-fold normalized to *Gapdh*) was detected in d18 dyn mESC-CMs when compared with d18 stat mESC-CMs. We identified a significant downregulation of sarco/endoplasmic reticulum calcium ATPase 2 (*Atp2a2,* normalized to *Gapdh*) expression in d18 dyn mESC-CMs. Interestingly, when normalized to *Rplp0*, we saw that *Atp2a2* was 1.5-fold upregulated in d18 dyn mESC-CMs when compared with the static controls. An increase in the expression of inward-rectifier potassium channel Kir2.2 (*Kcnj12*) and sodium voltage-gated channel alpha subunit (*Scn5a*) was observed in d18 dyn mESC-CMs (both normalized to *Gapdh* or *Rplp0*); however, no statistical significance was detected (Figure S3 and Table S1).

As shown before, Raman microspectroscopy allows the marker-free monitoring of cardiac maturation (Brauchle et al., 2016). Thus, Raman spectra of the 18-day statically and dynamically-cultured mESC-CMs were recorded and analyzed using principal component analysis (PCA). The loadings of the PC values exhibited spectral changes due to the different phenotypes. Plotting of PC-1 and PC-2 score values depicted two clearly distinguishable populations (Figure 2D). The investigation of the correlated PC-1 loading patterns elucidated a stronger impact of peaks at 860 cm^{-1} (glycogen), 938 cm^{-1} (glycogen), 1,003 cm^{-1} (phenylalanine), 1,123 cm^{-1} (glycogen), and 1,658 cm^{-1} (amide I) on the spectra of d18 dyn mESC-CMs when compared with those from d18 stat mESC-CMs. These peaks were all previously associated with postnatal maturation of CMs (Figure 2E; Notingher et al., 2004; Movasaghi et al., 2007; Pascut et al., 2013; Brauchle et al., 2016). In contrast, Raman peaks at 785 cm^{-1} (phosphodiester bonds of DNA) and 1,342 cm^{-1} (guanine) were more predominant in d18 stat mESC-CMs.

We further investigated the calcium-handling properties of d12 and d18 dyn mESC-CMs (Figures 3A–3D). No significant changes of the slope of Ca^{2+} transient and relative amplitude values were detected, whereas caffeine-induced transient duration time (CaT_{90}) and time constant (tau) were both significantly shorter in d18 dyn mESC-CMs when compared with d12 dyn mESC-CMs (Figure 3B). To quantify the sarcoplasmic reticulum (SR) stores and SERCA function, d12 and d18 dyn mESC-CMs were subjected to rapid puffs of a caffeine-containing solution. Typical caffeine-induced Ca^{2+} transients with a sharp peak followed by a gradual return to diastolic levels were detected (Figure 3C). An increase of CaT_{90} was observed in d18 dyn mESC-CMs (Figure 3D). The SERCA activity, which was calculated by subtracting the decay rate from the systolic Ca^{2+} transient as previously reported (Kosmidis et al., 2015), was significantly increased in d18 dyn mESC-CMs, indicating an enhanced SERCA function (Figure 3D).

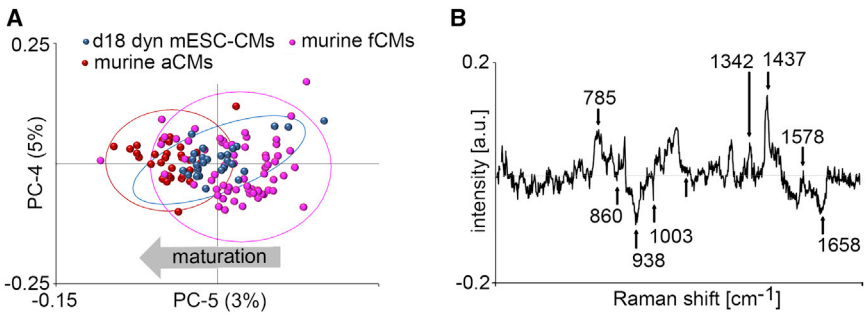

Figure 4. Phenotype Characterization of d18 dyn mESC-CMs Using Raman Micro-spectroscopy

(A) Scores plot demonstrates spectral changes due to cardiac maturation (n = 30 measurements from three independent cultures for d18 dyn mESC-CMs and murine aCMs, n = 60 measurements from three independent cultures for murine fCMs).

(B) Corresponding PC-5 loading spectrum describes the differences between the murine CM phenotypes. Arrows highlight the wavenumbers of the prominent differences.

d18 dyn mESC-CMs Express a Similar Phenotype to Adult Murine CMs

To further explore the maturation status of d18 dyn mESC-CMs, the Raman spectra of d18 dyn mESC-CMs were recorded and compared with the Raman spectra of murine fetal CMs (fCMs; age, embryonic day 15.5) and adult CMs (aCMs; age, 3 months) using PCA (Figure 4A). The cluster of d18 dyn mESC-CMs showed a partial overlap with the clusters of fCMs and aCMs. When analyzing the PC-5 loading, we identified that Raman bands at 860, 938, 1003, and 1,658 cm^{-1} were decreased, most likely due to the degree of maturation of the CMs (Figure 4B). The nucleic acid-specific bands at 785, 1,342, and 1,578 cm^{-1} (guanine and adenine), and the protein-specific band 1,437 (acyl chains in lipids) were more predominant in fCMs (Notingher et al., 2004; Movasaghi et al., 2007; Pascut et al., 2013).

Extended Dynamic Culture Significantly Increases Cardiac-Associated Protein and Gene Expression in hESC-CMs that Is Controlled by the Wnt/β-Catenin Pathway

To investigate the effect of an extended dynamic culture on cardiac maturation in hESC-CMs, we utilized a previously established protocol (Satin et al., 2004; Lundy et al., 2013; Brauchle et al., 2016). We chose days 10 and 20 for analyses since these time points have been previously reported to be crucial for early- and mid-stage assessment of cardiac maturation (Satin et al., 2004; Lundy et al., 2013; Brauchle et al., 2016). The differentiation efficiency using this protocol was confirmed by imaging flow cytometry (Figure S4). After 20 days of dynamic culture, 18.4% of the cells were $cTNT^+$; whereas only 7.2% of the cells were $cTNT^+$ in the static controls (Figure S4). Similar to our findings utilizing mESC-derived cells, IF staining showed well-defined, aligned, cross-striated MF20 and cTNT patterns in both CMs derived from day 10 (d10 dyn hESC-CMs) and day 20 (d20 dyn hESC-CMs) dynamically-cultured populations (Figure 5A). In contrast, no striated sarcomeric structures were seen in CMs derived from day 10 (d10 stat hESC-CMs) or day 20 (d20 stat hESC-CMs) static controls (Figure 5A). Aligned rod-shaped myofilaments were observed in d20 dyn hESC-CMs (Figure 5A). In contrast, d10 dyn hESC-CMs, as well as d10 and d20 stat hESC-CMs, exhibited random arrays of myofilaments (Figure 5A). CX43 staining in d10 dyn hESC-CMs and d20 stat hESC-CMs appeared diffuse (Figure 5A), whereas d20 dyn hESC-CMs displayed a strong CX43 expression along the sarcolemma or at the intercalated discs (Figure 5A). Overall, CX43 was more abundant in the d20 dyn hESC-CMs when compared with the d10 dyn hESC-CMs, or d10 and d20 stat hESC-CMs (Figure 5A). In addition, the sarcomere length of d20 dyn hESC-CMs was significantly increased when compared with d20 stat hESC-CMs and d10 dyn hESC-CMs (Figure 5B). Imaging flow cytometry was used to validate the IF staining data. ZR was used to select viable cells for cTNT expression analysis (Figure 5A). There was a statistically significant increase in the MFI of cTNT expression in the d20 dyn hESC-CMs when normalized to the d20 stat hESC-CMs (Figures 5C and 5D). We examined the cardiac-associated gene expression in d20 dyn hESC-CMs and compared it to d20 stat hESC-CMs (Figure S5 and Table S1). *MYH7* was significantly upregulated in d20 dyn hESC-CMs compared with d20 stat hESC-CMs (normalized to *RPLP0*). The expression of other cardiac-associate genes, such as α-actinin 2 (*ACTN2*), *TNNT2* and troponin I3 (*TNNI3*) were increased in d20 dyn hESC-CMs (normalized to either *GAPDH* or *RPLP0*); however, this increase was not statistically significant (Figure S5). It has been proposed that maturation of hESC-CMs is related to changes in ion channel expression, with relevant electrophysiological properties (Bosman et al., 2013). Expression of *CACNA1C* (5.6-fold normalized to *GAPDH*; 10.2-fold normalized to *RPLP0*) and *ATP2A2* (4.0-fold normalized to *GAPDH*; 6.9-fold normalized to *RPLP0*) increased significantly in d20 dyn hESC-CMs when compared with d20 stat hESC-CMs (Figure S5). No significant changes in the expression of sodium/potassium-related ion channels, including *SCN5A*, *HCN4*, *KCNH2*, and *KCNJ12*, and the slowly activating delayed-rectifier potassium channel

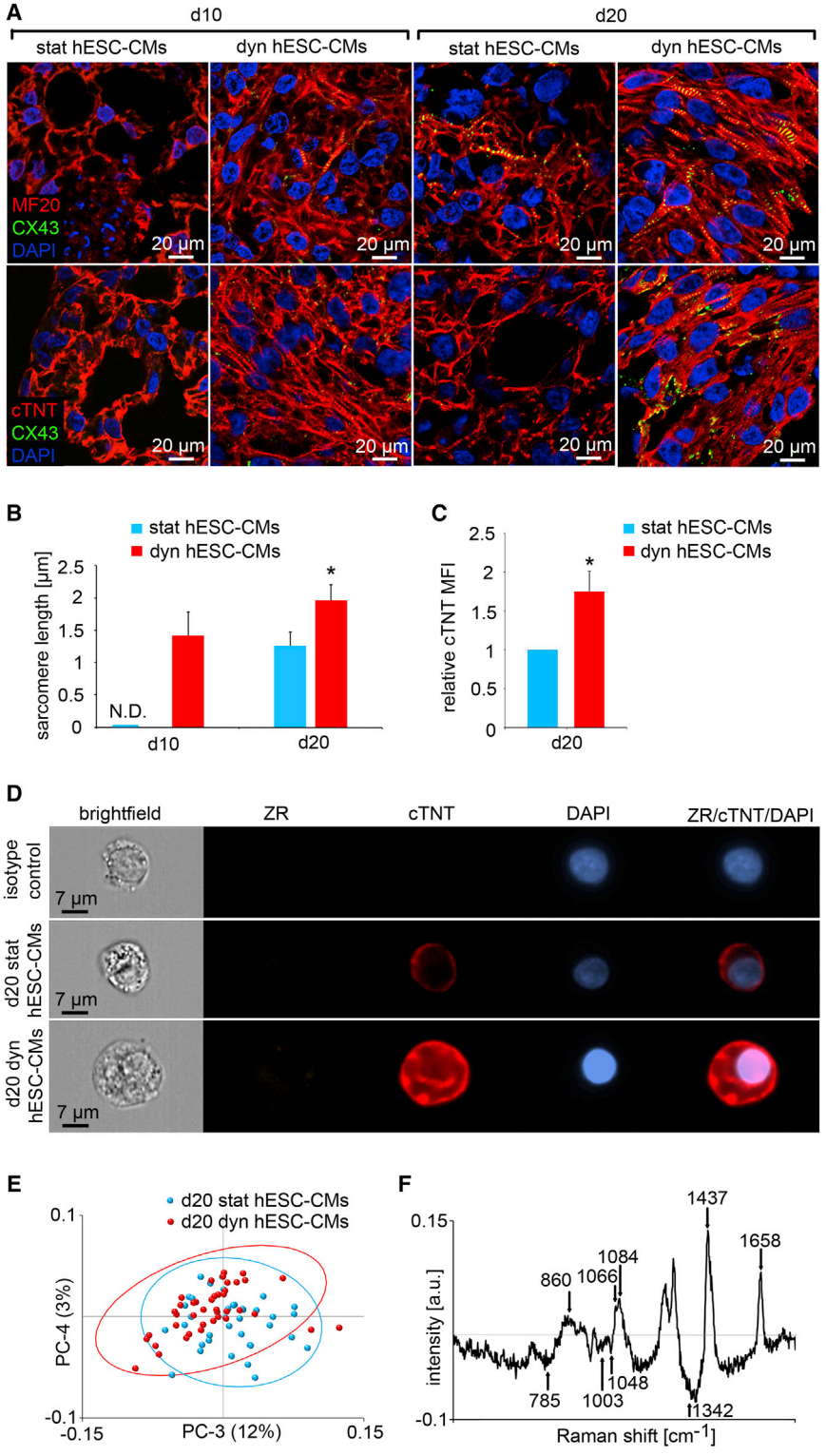

Figure 5. Mechanical Stimuli Induce an Enhanced Cardiac Protein Expression Pattern in hESC-CMs

(A) IF images show expression of MF20 (red), CX43 (green), cTNT (red), and DAPI (blue) in d10 stat and dyn, and d20 stat and dyn hESC-CMs.

(B) Quantification of sarcomere length in d10 and d20 hESC-CMs (n = 20 cells from three independent cultures each). Error bars show SD. N.D. = not detectable. *p < 0.01 versus stat hESC-CMs at the same time point.

(C) Relative MFI of cTNT expression in d20 stat and dyn hESC-CMs (n = 4). Error bars show SD. *p = 0.0014.

(D) Representative images of d20 stat and dyn hESC-CMs stained with ZR (orange), cTNT (red), and DAPI (blue). ZR/cTNT/DAPI represents an overlay.

(E) Scores of PC-3 and PC-4 of Raman spectra from d20 stat hESC-CMs (n = 30 measurements from three independent cultures) and d20 dyn hESC-CMs (n = 45 measurements from three independent cultures).

(F) PC-4 loadings represent Raman peaks that changed significantly in d20 dyn hESC-CMs when compared with static d20 stat hESC-CMs (see also Figures S4–S6).

subfamily (*KCNQ1*) were observed in d20 dyn hESC-CMs when normalized to *GAPDH*. In contrast, when normalized to *RPLP0*, we saw that *KCNJ12* (2.4-fold), *SCN5A* (4.1-fold), and *HCN4* (5.0-fold) were significantly upregulated in d20 dyn hESC-CMs when compared with d20 stat hESC-CMs (Figure S5).

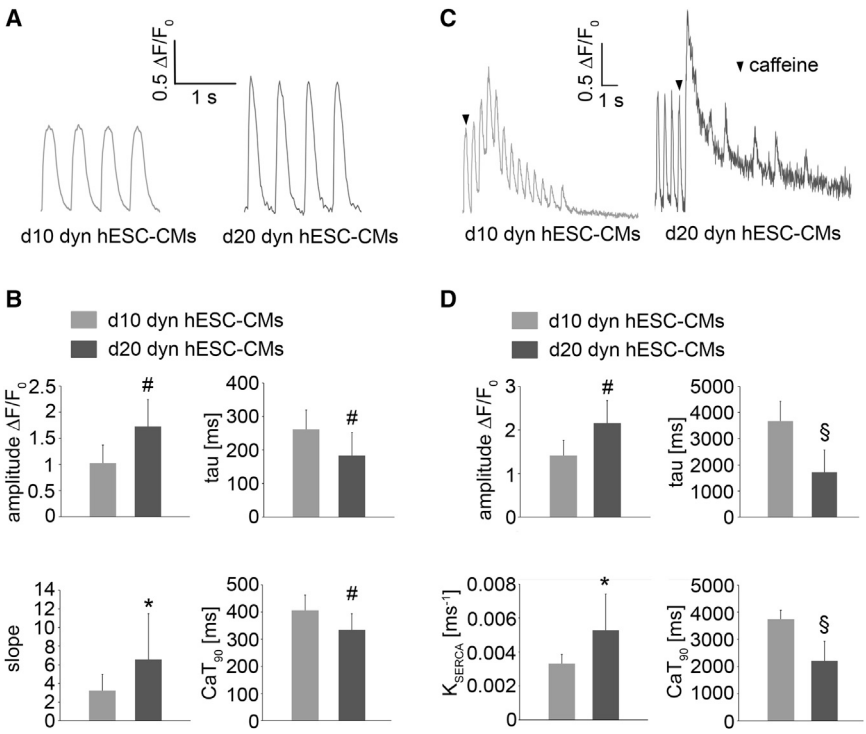

Figure 6. Assessment of Calcium Transient Properties in Dynamically-Cultured hESC-CMs

(A) Typical systolic Ca^{2+} transient traces of d10 and d20 dyn hESC-CMs stimulated at the frequency of 2 Hz.

(B) Average amplitude, time constant of decay (tau), slope, and Ca^{2+} transient duration (CaT_{90}) in d10 (n = 8) and d20 (n = 12) dyn hESC-CMs. Error bars show SD.

(C) Recording of caffeine-induced Ca^{2+} transient in d10 and d20 dyn hESC-CMs.

(D) Average caffeine-induced amplitude, time constant of decay (tau), SERCA activity, and CaT_{90} in d10 (n = 8) and d20 dyn (n = 12) hESC-CMs. Error bars show SD.

*p < 0.05, #p < 0.05, §p < 0.001 (see also Figure S7).

We acquired and compared Raman spectral fingerprints of d20 stat and d20 dyn hESC-CMs (Figure 5E). Although PC score plots depicted two distinct populations, an intermediate zone was also visible where both populations overlapped. The responsible peaks for the population separation were 785, 860, 1,003, 1,048 (glycogen), 1,066 (cholesterol), 1,084 (glycogen), 1,342, 1,437, and 1,658 cm^{-1} (Figure 5E). d20 dyn hESC-CMs exhibited stronger signals at 860, 1,066, 1,084, 1,437, and 1,658 cm^{-1} (Brauchle et al., 2016). Signals at 785, 1,003, 1,048, and 1,342 cm^{-1} were more pronounced in Raman spectra of d20 stat hESC-CMs (Figure 5F).

The Wnt/β-catenin signaling pathway has been shown to play a prominent role in regulating cardiogenesis (Hurlstone et al., 2003; Naito et al., 2006; Tzahor, 2007; Alfieri et al., 2010; Gessert and Kühl, 2010; Piven et al., 2014). In the early phase of cardiogenesis, the activation of Wnt/β-catenin signaling promotes the commitment of mesodermal cells to the cardiac lineage, which is in great contrast to the late phase of cardiac development, where a downregulation of β-catenin promotes the maturation of committed CMs (Naito et al., 2006). Based on these studies, we examined whether this pathway also mediates the mechanical stimuli-induced hESC-CM maturation. As depicted in Figure S6, d20 dyn hESC-CMs expressed a lower level of β-catenin compared with d20 stat hESC-CMs, indicating an inhibition of the Wnt/β-catenin signaling pathway due to the impact of mechanical forces.

Dynamically-Cultured hESC-CMs Exhibit Proper Cardiac Electrophysiology and Ca^{2+} Handling

Ca^{2+} handling was assessed in d10 and d20 dyn hESC-CMs paced at 2 Hz. Typical systolic Ca^{2+} transient traces were recorded in both d10 and d20 dyn hESC-CMs (Figure 6A). When compared with d10 dyn hESC-CMs, the d20 dyn hESC-CMs showed a significantly higher transient amplitude, a higher slope, a shorter CaT_{90}, and a smaller time constant (Figure 6B). To investigate the SR storage and release capacity, caffeine puffs (10 mM) were applied to d10 and d20 dyn hESC-CMs (Figure 6C). Both d10 and d20 dyn hESC-CMs exhibited caffeine-releasable SR Ca^{2+} stores (Figure 6C). The caffeine-induced Ca^{2+} transient amplitude in d20 dyn hESC-CMs was higher when compared with d10 dyn hESC-CMs, suggesting an increased SR storage capacity in the d20 dyn hESC-CMs (Figure 6D). d20 dyn hESC-CMs also exhibited a decrease in CaT_{90} and a faster transient decay (Figure 6D). SERCA activity was significantly increased in d20 dyn hESC-CMs, indicating an enhanced SERCA function.

Nifedipine, an L-type calcium channel blocker, induced a dose-dependent shortening of the field action potential duration (fPd) in d10 stat and dyn, as well as d20 stat and dyn hESC-CMs (Figures S7A and S7B). The shortening of the fPd was initiated at 10 nM and saturated at 1 μM (Figure S7A). No significant differences in response to nifedipine were detected in static versus dynamic hESC-CMs. When exposed to the hERG K^+ channel blocker dofetilide,

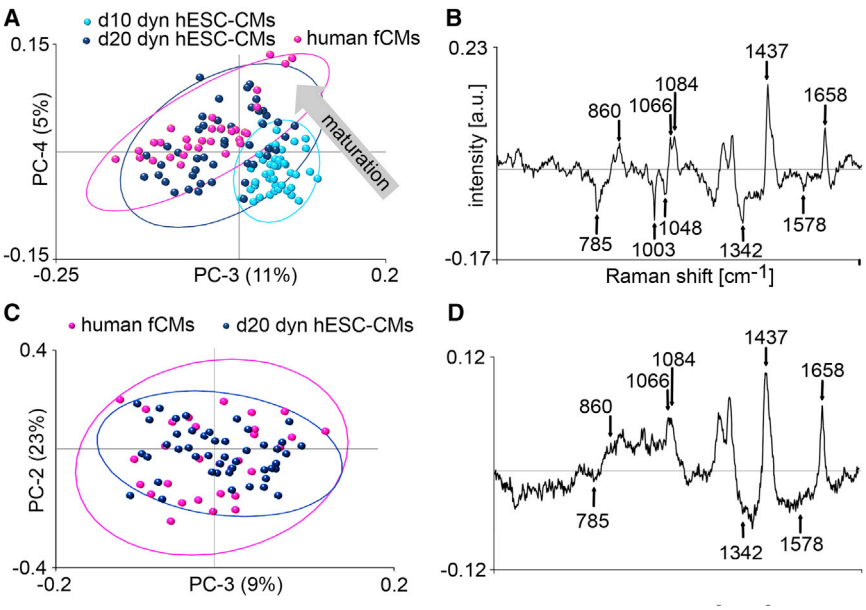

Figure 7. Raman Microspectroscopic Analysis of Dynamically-Cultured hESC-CMs

(A) Scores plot of human fCMs (n = 30 measurements from three independent cultures), d10 dyn (n = 30 measurements from three independent cultures) and d20 dyn hESC-CMs (n = 45 measurements from three independent cultures).

(B) Corresponding PC-4 loading spectrum describes the differences between the CM phenotypes.

(C) Scores plot of human fCMs (n = 30 measurements from three independent cultures) and d20 dyn hESC-CMs (n = 45 measurements from three independent cultures).

(D) Corresponding loading spectrum describes the differences between the CM phenotypes.

all hESC-CMs displayed a dose-dependent prolongation of fPd (Figures S7C and S7D), which was seen previously by others (Harris et al., 2013). Dofetilide is known as a high-risk drug to evoke arrhythmia of the torsade-de-pointes type (Jaiswal and Goldbarg, 2014). Interestingly, in some of the measurements, we observed that dofetilide induced early after depolarizations in hESC-CMs at higher concentrations.

Phenotype Characterization of Dynamically-Cultured hESC-CMs

To identify maturation stages of dynamically-cultured hESC-CMs, the Raman spectra of d10 and d20 dyn hESC-CMs were compared with the Raman spectra of primary isolated human fCMs (Figure 7A). The loading spectrum of PC-4 highlights that the observed bands at 785, 1,003, 1,048, 1,342, and 1,578 cm^{-1} decreased, and the bands at 860, 1,066, 1,084, 1,437, and 1,658 cm^{-1} increased, due to the stage of maturation of the CMs (Figure 7B), which is similar to what had been reported previously by others (Notingher et al., 2004; Movasaghi et al., 2007). Interestingly, PCA of d20 dyn hESC-CMs and human fCMs alone revealed molecular similarities of the two cell types (Figures 7C and 7D).

DISCUSSION

Mechanical signals play a crucial regulatory role in cardiac growth, development, and maintenance (Happe and Engler, 2016). Here, we developed a bioreactor system that exposes ESC-derived cells to defined pulsatile flow and cyclic strain, thereby mimicking in vivo physical signals that are important for normal cardiac development (Andrés-Delgado and Mercader, 2016). Compared with other recent bioreactor-related studies, which focused on either using cyclic strain or cyclic strain and electrical stimulation (Torsoni et al., 2005; Gwak et al., 2008; Tulloch et al., 2011; Huang et al., 2012; Nunes et al., 2013; Mihic et al., 2014), we highlight the importance of combining pulsatile flow and cyclic stain to drive ESC-CM maturation in vitro. The applied shear stresses induced by pulsatile flow in this study ($\sim 10^{-2}$ to 10^{-3} dyn/cm^2) differ from physiological blood luminal flow ($\sim$10–20 dyn/cm^2) (Butcher and Nerem, 2007; Chiu and Chien, 2011), but instead correspond to the in vivo environment, where CMs are exposed to an extremely low transmural flow rather than direct shear stress (Andrés-Delgado and Mercader, 2016). Of note, cardiac wall strains display significant temporal and regional variations ($-7.9\% \pm 3.8\%$ to $+11.3\% \pm 6.4\%$ in vivo [Tsamis et al., 2011]). To mimic cardiac strain, previous studies applied cyclic strain between 2.5% and 12% to PSC-CMs, and demonstrated that cyclic strain conditioning can increase the expression of cardiac-associated markers and improve organization of sarcomere proteins (Shyu et al., 2010; Huang et al., 2012; Mihic et al., 2014). In accordance with these studies, culturing mESC-derived cells for 12 days in the presence of cyclic strains alone led to a significant upregulation of cardiac-associated genes and an increased number of $MF20^+$ cells when compared with static controls. We further observed a synergistic effect of the combination of 1.48 mL/min pulsatile flow with 5% cyclic strain, which led to a significant increase of cardiac-associated gene expression and an improved alignment of

sarcomeric fibers. When then extending the culture time, markers associated with CM maturation were further increased in both murine and human ESC-CMs. In detail, d18 dyn mESC-CMs and d20 dyn hESC-CMs displayed well-organized sarcomeric proteins, a higher gap junction protein expression, and an increased cardiac ion channel gene expression. d20 dyn hESC-CMs exhibited an average sarcomere length of 1.97 ± 0.25 μm, which is higher than the average sarcomere length of hESC-CMs reported in other studies and similar to the sarcomere length of relaxed adult CMs (Borg et al., 2000; Feinberg et al., 2013; Nunes et al., 2013). Maturation of ESC-CMs is often accompanied by increased ion channel expression. Our data showed an increase in relevant ion channel genes in d18 dyn mESC-CMs and d20 dyn hESC-CMs when compared with d18 stat mESC-CMs or d20 stat hESC-CMs (normalized to either *Gapdh* [mouse]/*GAPDH* [human], or *Rplp0* [mouse]/*RPLP0* [human]). Raman microspectroscopy was employed in a previous study for the marker-free characterization of different CM phenotypes (Brauchle et al., 2016). Here, we compared Raman spectra and identified that structural protein- and lipid-related peaks were more prominent in d18 dyn mESC-CMs when compared with d18 stat mESC-CMs. The stronger protein-related peaks in d18 dyn mESC-CMs had been previously identified as glycogen (Pascut et al., 2011, 2013). A higher presence of glycogen in ESC-CMs was previously attributed to an increased glycolytic metabolism in CMs, which is required to produce myofibril contractions (Pascut et al., 2011, 2013). Lipids have been described to play an important role in energy storage and homeostasis in cardiac muscle (Chung et al., 2007). The increase in lipid-related bands in d18 dyn mESC-CMs might be attributed to a metabolic shift toward β-oxidation of fatty acids (Chung et al., 2007; Brauchle et al., 2016). The comparison of mESC-CMs and primary isolated fCMs and aCMs revealed that d18 dyn mESC-CMs exhibited a phenotype closer to murine aCMs. Similar to murine aCMs, human aCMs exhibit a lower nuclear and higher mitochondrial density as well as a metabolic shift (Pohjoismaki et al., 2013). In accordance, d20 dyn hESC-CMs and human fCMs showed stronger structural protein- and lipid-related peak intensities, but decreased signals of nucleotide bands when compared with hESC-CMs cultured for only 10 days or under static conditions. The observed differences in protein-assigned bands are possibly due to the sarcomeric organization and increasing myofibril densities in the d20 dyn hESC-CMs, as was confirmed by IF staining in this study and as hypothesized previously (Brauchle et al., 2016). These findings highlight the importance of combined pulsatile flow and cyclic strain in the maturation process of PSC-CMs.

In our study, we revealed that d18 dyn mESC-CMs and d20 dyn hESC-CMs showed a functional improvement as the typical systolic calcium transient parameters, the rate of constant of Ca^{2+} decay (tau), slope, and amplitude improved with extended culture times, indicating rapid electromechanical coupling. This change could be the result of structural changes in the contractile apparatus, the better orientation of the myocyte network associated with enhanced expression of gap junctions, or alterations in the balance of cardiac ion channels (Zhu et al., 2014). In previous studies, most of the ESC-CMs did not respond to caffeine as they relied on calcium influx from sarcolemma instead of the SR as seen in adult CMs (Khan et al., 2013; Li et al., 2013). In a few studies, hESC-CMs cultured for more than 27 days showed a response to caffeine (Nunes et al., 2013; Kosmidis et al., 2015). Here, ESC-CMs responded to caffeine after 12 (mESC-CMs) or 10 days (hESC-CMs), as shown by an increased Ca^{2+} handling consistent with a functional SR. Furthermore, when compared with d12 dyn mESC-CMs and d10 hESC-CMs, d18 dyn mESC-CMs and d20 dyn hESC-CMs exhibited a higher store of Ca^{2+} and an improved SERCA function. We further performed concentration-response studies employing nifedipine and dofetilide. Although hESC-CMs exhibited a dose-dependent response to nifedipine and dofetilide, no significant differences were seen between stat and dyn hESC-CMs. The electrophysiology was stable throughout the recordings. This indicates that the calcium and hERG channels in all hESC-CMs were fully functional without any limitation.

In concert with biochemical cues, mechanical stimuli can activate or inhibit signaling pathways, and thus regulate transcription factor expression to drive myocardial differentiation, specification, and maturation (Van Vliet et al., 2012; Happe and Engler, 2016). As shown by others (Gessert and Kühl, 2010), we also detected a lower expression of β-catenin in d20 dyn hESC-CMs when compared with d20 stat hESC-CMs. Wnt/β-catenin signaling has been reported to have a stage-dependent, paradoxical effect on cardiogenesis. We hypothesize that the low expression of β-catenin seen in d20 dyn hESC-CMs was due to late-phase cardiac maturation (Gessert and Kühl, 2010). A stretch-induced downregulation of Wnt/β-catenin was described in other studies using human osteoblastic cells (Jansen et al., 2010). The Wnt/β-catenin signaling pathway is one of many pathways regulated by mechanical stimuli. Other mechanically-induced signaling pathways may also play a role in regulating cardiac differentiation and maturation (Fonseca et al., 2005; Torsoni et al., 2005; Jaalouk and Lammerding, 2009). Future work will focus on the systematical identification of the signaling pathways that are activated when applying different mechanical stimuli. In addition, development of the existing bioreactor toward a high-throughput system would be beneficial since this would allow studies with increased numbers of experimental

conditions and replicates while reducing the amounts of required cell and culture materials.

EXPERIMENTAL PROCEDURES

Full experimental procedures are provided in the Supplemental Information.

Design and Simulation of a Multi-functional Bioreactor System

A custom-built, bioreactor system was designed using SolidWorks for CAD (SolidWorks 2010, Dassault Systemes SolidWorks). It is composed of an air and fluid chamber that are separated by a silicone membrane in order to ensure a sterile environment (Figure 1). A computational model was developed to assess the designed bioreactor system performance in silico. Meshing and calculations were performed in COMSOL 4.3a based on the bioreactor geometry and dimensions (COMSOL Multiphysics). The detailed experimental setup description is provided in the Supplemental Information.

mESC and hESC Cultures

CCE mESCs and H9 hESCs were employed in this study. The use of hESCs for this study was approved by the Robert Koch Institute, Berlin (AZs: 3.04.02/0086 and 3.04.02/0111). For experiments, 1.18×10^6 CCE mESCs/9.5 cm^2 were seeded on the center area of fibronectin-coated ThinCert six-well culture inserts (Greiner Bio-One), followed by transfer into the bioreactor system and exposure to pulsatile flow-induced shear stress or/and strain for 12 or 18 days. hESC differentiation was performed based on a protocol that was previously reported (Brauchle et al., 2016). After 4 days of differentiation, 200 EBs/9.5 cm^2 were seeded on the center of gelatin-coated ThinCert inserts, which were subsequently transferred into the bioreactor and exposed to pulsatile flow-induced shear stress and strain for 5 or 15 days (in total d10 and d20 of culture, counted from the undifferentiated cell stage). See the Supplemental Information for details.

IF Staining

All cells were fixed directly on the membranes with 4% paraformaldehyde (PFA). The mESC-CMs were further processed for staining as described previously (Hinderer et al., 2015). For hESC-CMs samples, HistoGel (American MasterTech) was dispensed on the samples after PFA was removed, followed by embedding in paraffin. IF staining of 3 μm sections was performed as described previously (Votteler et al., 2013). All antibodies are listed in the Supplemental Information. DAPI was used to visualize cell nuclei. An LSM710 confocal microscope (Carl Zeiss) was used for imaging. Sarcomere length was analyzed using ImageJ (version 1.46r, Wayne Rasband, NIH) (Wang et al., 2013; Nance et al., 2015).

Calcium Transient Recordings

mESC-CMs and hESC-CMs were transferred to fibronectin-coated, plastic-bottom Petri dishes and the fluorescence intensity of Ca520-AM dye was measured using a Confocal LSM710 microscope with a controlled temperature of 37°C and 5% CO_2. Electrical field stimulation was applied to evoke Ca^{2+} transients at the stimulation frequencies of 3 Hz (hESC-CMs) or 2 Hz (hESC-CMs) using bipolar electrodes attached to an STG-2004 stimulator (Multi Channel Systems [MCS]). Systolic and caffeine-induced Ca^{2+} transient duration (from peak amplitude until 90% return to base level, CaT_{90}), decay, amplitude, and slope were assessed as published previously (Kosmidis et al., 2015).

Raman Microspectroscopy

A custom-built Raman microspectroscope was used to acquire Raman spectra of mESC-CMs and hESC-CMs as described previously in detail (Brauchle et al., 2016). A detailed description of the experimental setup, including Raman spectra processing and PCA is provided in the Supplemental Information. Additional details on these pre-processing steps were described previously in detail (Pudlas et al., 2011; Votteler et al., 2012a, 2012b; Brauchle et al., 2014, 2016).

Statistical Analysis

Except stated otherwise, data are shown in mean ± SD. One-way ANOVA was performed to compare data groups. Student's t test was performed to compare between two data groups. A probability value of 95% ($p < 0.05$) was used to determine significance.

SUPPLEMENTAL INFORMATION

Supplemental Information includes Supplemental Experimental Procedures, seven figures, and one table and can be found with this article online at http://dx.doi.org/10.1016/j.stemcr.2017.04.021.

AUTHOR CONTRIBUTIONS

N.S., E.B., U.K., and K.S.-L. designed the experiments. N.S. and J.R. designed the bioreactor. N.S., A.K., C.W., U.K., H.B., S.P., and S.K. performed experiments, and collected and analyzed the data. S.L.L., M.H., and A.N. gave conceptual advice. N.S., S.H., S.L.L., and K.S.-L. wrote the manuscript.

ACKNOWLEDGMENTS

We thank Adrienne Lee (Fraunhofer IGB) for her assistance with the Raman measurements. This work was financially supported by CIRM (RB3-05086 to A.N.), Fraunhofer-Gesellschaft (Attract to K.S.-L., FFE to S.L.L., and Talenta to S.H.), DAAD RISE and US Fulbright Student Scholarships (both to J.R.), as well as the BMBF (0316059), Ministry of Science, Research and Arts of Baden-Württemberg (Az.: SI-BW 01222-91, 33-729.55-3/214), and the DFG (INST 2388/33-1, SCHE 701/7-1, SCHE 701/10-1) (all to K.S.-L).

Received: June 18, 2016
Revised: April 19, 2017
Accepted: April 20, 2017
Published: May 18, 2017

REFERENCES

Alfieri, C.M., Cheek, J., Chakraborty, S., and Yutzey, K.E. (2010). Wnt signaling in heart valve development and osteogenic gene induction. Dev. Biol. *338*, 127–135.

Andrés-Delgado, L., and Mercader, N. (2016). Interplay between cardiac function and heart development. Biochim. Biophys. Acta *1863*, 1707–1716.

Blazeski, A., Zhu, R., Hunter, D.W., Weinberg, S.H., Boheler, K.R., Zambidis, E.T., and Tung, L. (2012). Electrophysiological and contractile function of cardiomyocytes derived from human embryonic stem cells. Prog. Biophys. Mol. Biol. *110*, 178–195.

Borg, T.K., Goldsmith, E.C., Price, R., Carver, W., Terracio, L., and Samarel, A.M. (2000). Specialization at the Z line of cardiac myocytes. Cardiovasc. Res. *46*, 277–285.

Bosman, A., Sartiani, L., Spinelli, V., Del Lungo, M., Stillitano, F., Nosi, D., Mugelli, A., Cerbai, E., and Jaconi, M. (2013). Molecular and functional evidence of HCN4 and caveolin-3 interaction during cardiomyocyte differentiation from human embryonic stem cells. Stem Cells Dev. *22*, 1717–1727.

Braam, R., Passier, R., and Mummery, C.L. (2009). Cardiomyocytes from human pluripotent stem cells in regenerative medicine and drug discovery. Trends Pharmacol. Sci. *30*, 536–545.

Brauchle, E., Thude, S., Brucker, S.Y., and Schenke-Layland, K. (2014). Cell death stages in single apoptotic and necrotic cells monitored by Raman microspectroscopy. Sci. Rep. *4*, 4698.

Brauchle, E., Knopf, A., Bauer, H., Shen, N., Linder, S., Monaghan, M.G., Ellwanger, K., Layland, S.L., Brucker, S.Y., Nsair, A., et al. (2016). Novel non-invasive identification of chamber specific cardiomyocytes in differentiating pluripotent stem cells. Stem Cell Rep. *6*, 188–199.

Butcher, J.T., and Nerem, R.M. (2007). Valvular endothelial cells and the mechanoregulation of valvular pathology. Philos. Trans. R Soc. Lond B Biol. Sci. *362*, 1445–1457.

Carrier, R.L., Rupnick, M., Langer, R., Schoen, F.J., Freed, L.E., and Vunjak-Novakovic, G. (2002). Perfusion improves tissue architecture of engineered cardiac muscle. Tissue Eng. *8*, 175–188.

Chiu, J.J., and Chien, S. (2011). Effects of disturbed flow on vascular endothelium: pathophysiological basis and clinical perspectives. Physiol. Rev. *91*, 327–387.

Chung, S., Dzeja, P.P., Faustino, R.S., Perez-Terzic, C., Behfar, A., and Terzic, A. (2007). Mitochondrial oxidative metabolism is required for the cardiac differentiation of stem cells. Nat. Clin. Pract. Cardiovasc. Med. *4*, S60–S67.

Davis, R.P., Casini, S., van den Berg, C.W., Hoekstra, M., Remme, C.A., Dambrot, C., Salvatori, D., Oostwaard, D.W., Wilde, A.A., Bezzina, C.R., et al. (2012). Cardiomyocytes derived from pluripotent stem cells recapitulate electrophysiological characteristics of an overlap syndrome of cardiac sodium channel disease. Circulation *125*, 3079–3091.

Ebert, A.D., Liang, P., and Wu, J.C. (2012). Induced pluripotent stem cells as a disease modeling and drug screening platform. J. Cardiovasc. Pharmacol. *60*, 408–416.

Feinberg, A.W., Ripplinger, C.M., van der Meer, P., Sheehy, S.P., Domian, I., Chien, K.R., and Parker, K.K. (2013). Functional differences in engineered myocardium from embryonic stem cell-derived versus neonatal cardiomyocytes. Stem Cell Rep. *1*, 387–396.

Fonseca, P.M., Inoue, R.Y., Kobarg, C.B., Crosara-Alberto, D.P., Kobarg, J., and Franchini, K.G. (2005). Targeting to C-terminal myosin heavy chain may explain mechanotransduction involving focal adhesion kinase in cardiac myocytes. Circ. Res. *96*, 73–81.

Gessert, S., and Kühl, M. (2010). The multiple phases and faces of Wnt signaling during cardiac differentiation and development. Circ. Res. *107*, 186–199.

Guan, J., Wang, F., Li, Z., Chen, J., Guo, X., Liao, J., and Moldovan, N.I. (2011). The stimulation of the cardiac differentiation of mesenchymal stem cells in tissue constructs that mimic myocardium structure and biomechanics. Biomaterials *32*, 5568–5580.

Gwak, S.J., Bhang, S.H., Kim, I.K., Kim, S.S., Cho, S.W., Jeon, O., Yoo, K.J., Putnam, A.J., and Kim, B.S. (2008). The effect of cyclic strain on embryonic stem cell-derived cardiomyocytes. Biomaterials *29*, 844–856.

Happe, C.L., and Engler, A.J. (2016). Mechanical forces reshape differentiation cues that guide cardiomyogenesis. Circ. Res. *118*, 296–310.

Harris, K., Aylott, M., Cui, Y., Louttit, J.B., McMahon, N.C., and Sridhar, A. (2013). Comparison of electrophysiological data from human-induced pluripotent stem cell-derived cardiomyocytes to functional preclinical safety assays. Toxicol. Sci. *134*, 412–426.

Hinderer, S., Shena, N., Ringuette, L.J., Hansmann, J., Reinhardt, D.P., Brucker, S.Y., Davis, E.C., and Schenke-Layland, K. (2015). In vitro elastogenesis: instructing human vascular smooth muscle cells to generate an elastic fiber-containing extracellular matrix scaffold. Biomed. Mater. *10*, 034102.

Huang, Y., Zheng, L., Gong, X., Jia, X., Song, W., Liu, M., and Fan, Y. (2012). Effect of cyclic strain on cardiomyogenic differentiation of rat bone marrow derived mesenchymal stem cells. PLoS One *7*, e34960.

Hurlstone, A.F., Haramis, A.P., Wienholds, E., Begthel, H., Korving, J., Van Eeden, F., Cuppen, E., Zivkovic, D., Plasterk, R.H., and Clevers, H. (2003). The Wnt/beta-catenin pathway regulates cardiac valve formation. Nature *425*, 633–637.

Jaalouk, D.E., and Lammerding, J. (2009). Mechanotransduction gone awry. Nat. Rev. Mol. Cell Biol. *10*, 63–73.

Jaiswal, A., and Goldbarg, S. (2014). Dofetilide induced torsade de pointes: mechanism, risk factors and management strategies. Indian Heart J. *66*, 640–648.

Jansen, J.H., Eijken, M., Jahr, H., Chiba, H., Verhaar, J.A., van Leeuwen, J.P., and Weinans, H. (2010). Stretch-induced inhibition of Wnt/beta-catenin signaling in mineralizing osteoblasts. J. Orthop. Res. *28*, 390–396.

Khan, J.M., Lyon, A.R., and Harding, S.E. (2013). The case for induced pluripotent stem cell-derived cardiomyocytes in pharmacological screening. Br. J. Pharmacol. *169*, 304–317.

Kosmidis, G., Bellin, M., Ribeiro, M.C., van Meer, B., Ward-van Oostwaard, D., Passier, R., Tertoolen, L.G.J., Mummery, C.L., and Casini, S. (2015). Altered calcium handling and increased contraction force in human embryonic stem cell derived cardiomyocytes following short term dexamethasone exposure. Biochem. Biophys. Res. Commun. *467*, 998–1005.

Li, S., Chen, G., and Li, R.A. (2013). Calcium signalling of human pluripotent stem cell-derived cardiomyocytes. J. Physiol. *591*, 5279–5290.

Lundy, S.D., Zhu, W.Z., Regnier, M., and Laflamme, M.A. (2013). Structural and functional maturation of cardiomyocytes derived from human pluripotent stem cells. Stem Cells Dev. *22*, 1991–2002.

Masumoto, H., Matsuo, T., Yamamizu, K., Uosaki, H., Narazaki, G., Katayama, S., Marui, A., Shimizu, T., Ikeda, T., Okano, T., et al. (2012). Pluripotent stem cell-engineered cell sheets reassembled with defined cardiovascular populations ameliorate reduction in infarct heart function through cardiomyocyte-mediated neovascularization. Stem Cells *30*, 1196–1205.

Mihic, A., Li, J., Miyagi, Y., Gagliardi, M., Li, S.H., Zu, J., Weisel, R.D., Keller, G., and Li, R.K. (2014). The effect of cyclic stretch on maturation and 3D tissue formation of human embryonic stem cell-derived cardiomyocytes. Biomaterials *35*, 2798–2808.

Movasaghi, Z., Rehman, S., and Rehman, I.U. (2007). Raman spectroscopy of biological tissues. Appl. Spectrosc. Rev. *42*, 493–541.

Naito, A.T., Shiojima, I., Akazawa, H., Hidaka, K., Morisaki, T., Kikuchi, A., and Komuro, I. (2006). Developmental stage-specific biphasic roles of Wnt/β-catenin signaling in cardiomyogenesis and hematopoiesis. Proc. Natl. Acad. Sci. USA *103*, 19812–19817.

Nance, M.E., Whitfield, J.T., Zhu, Y., Gibson, A.K., Hanft, L.M., Campbell, K.S., Meininger, G.A., McDonald, K.S., Segal, S.S., and Domeier, T.L. (2015). Attenuated sarcomere lengthening of the aged murine left ventricle observed using two-photon fluorescence microscopy. Am. J. Physiol. Heart Circ. Physiol. *309*, H918–H925.

Notingher, I., Green, C., Dyer, C., Perkins, E., Hopkins, N., Lindsay, C., and Hench, L.L. (2004). Discrimination between ricin and sulphur mustard toxicity in vitro using Raman spectroscopy. J. R. Soc. Interf. *1*, 79–90.

Nunes, S.S., Miklas, J.W., Liu, J., Aschar-Sobbi, R., Xiao, Y., Zhang, B., Jiang, J., Masse, S., Gagliardi, M., Hsieh, A., et al. (2013). Biowire: a platform for maturation of human pluripotent stem cell-derived cardiomyocytes. Nat. Methods *10*, 781–787.

Pascut, F.C., Goh, H.T., Welch, N., Buttery, L.D., Denning, C., and Notingher, I. (2011). Noninvasive detection and imaging of molecular markers in live cardiomyocytes derived from human embryonic stem cells. Biophys. J. *100*, 251–259.

Pascut, F.C., Kalra, S., George, V., Welch, N., Denning, C., and Notingher, I. (2013). Non-invasive label-free monitoring the cardiac differentiation of human embryonic stem cells in-vitro by Raman spectroscopy. Biochim. Biophys. Acta *1830*, 3517–3524.

Passier, R., van Laake, L.W., and Mummery, C.L. (2008). Stem-cell-based therapy and lessons from the heart. Nature *453*, 322–329.

Piven, O.O., Palchevska, O.L., and Lukash, L.L. (2014). The Wnt/beta-catenin signaling in embryonic cardiogenesis, postnatal development and myocardium reconstruction. Tsitol. Genet. *48*, 72–83.

Pohjoismaki, J.L.O., Kruger, M., Al-Furoukh, N., Lagerstedt, A., Karhunen, P.J., and Braun, T. (2013). Postnatal cardiomyocyte growth and mitochondrial reorganization cause multiple changes in the proteome of human cardiomyocytes. Mol. Biosyst. *9*, 1210–1219.

Pudlas, M., Berrio, D.A.C., Votteler, M., Koch, S., Thude, S., Walles, H., and Schenke-Layland, K. (2011). Non-contact discrimination of human bone marrow-derived mesenchymal stem cells and fibroblasts using Raman spectroscopy. Med. Laser Appl. *26*, 119–125.

Ribeiro, M.C., Tertoolen, L.G., Guadix, J.A., Bellin, M., Kosmidis, G., D'Aniello, C., Monshouwer-Kloots, J., Goumans, M.J., Wang, Y.L., Feinberg, A.W., et al. (2015). Functional maturation of human pluripotent stem cell derived cardiomyocytes in vitro – correlation between contraction force and electrophysiology. Biomaterials *51*, 138–150.

Satin, J., Kehat, I., Caspi, O., Huber, I., Arbel, G., Itzhaki, I., Magyar, J., Schroder, E.A., Perlman, I., and Gepstein, L. (2004). Mechanism of spontaneous excitability in human embryonic stem cell derived cardiomyocytes. J. Physiol. *559*, 479–496.

Shyu, K.G., Wang, B.W., Lin, C.M., and Chang, H. (2010). Cyclic stretch enhances the expression of Toll-like receptor 4 gene in cultured cardiomyocytes via p38 MAP kinase and NF-κB pathway. J. Biomed. Sci. *17*, 1–13.

Taber, L.A. (2001). Biomechanics of cardiovascular development. Annu. Rev. Biomed. Eng. *3*, 1–25.

Torsoni, A.S., Marin, T.M., Velloso, L.A., and Franchini, K.G. (2005). RhoA/ROCK signaling is critical to FAK activation by cyclic stretch in cardiac myocytes. Am. J. Physiol. Heart Circ. Physiol. *289*, H1488–H1496.

Tsamis, A., Bothe, W., Kvitting, J.-P., Swanson, J.C., Miller, D.C., and Kuhl, E. (2011). Active contraction of cardiac muscle: in vivo characterization of mechanical activation sequences in the beating heart. J. Mech. Behav. Biomed. Mater. *4*, 1167–1176.

Tulloch, N.L., Muskheli, V., Razumova, M.V., Korte, F.S., Regnier, M., Hauch, K.D., Pabon, L., Reinecke, H., and Murry, C.E. (2011). Growth of engineered human myocardium with mechanical loading and vascular coculture. Circ. Res. *109*, 47–59.

Tzahor, E. (2007). Wnt/beta-catenin signaling and cardiogenesis: timing does matter. Dev. Cell *13*, 10–13.

Van Vliet, P., Wu, S.M., Zaffran, S., and Puceat, M. (2012). Early cardiac development: a view from stem cells to embryos. Cardiovasc. Res. *96*, 352–362.

Votteler, M., Carvajal Berrio, D.A., Pudlas, M., Walles, H., and Schenke-Layland, K. (2012a). Non-contact, label-free monitoring of cells and extracellular matrix using Raman spectroscopy. J. Vis. Exp. http://dx.doi.org/10.3791/3977.

Votteler, M., Carvajal Berrio, D.A., Pudlas, M., Walles, H., Stock, U.A., and Schenke-Layland, K. (2012b). Raman spectroscopy for the non-contact and non-destructive monitoring of collagen damage within tissues. J. Biophotonics *5*, 47–56.

Votteler, M., Carvaja Berrio, D.A., Horke, A., Sabatier, L., Reinhardt, D.P., Nsair, A., Aikawa, E., and Schenke-Layland, K. (2013). Elastogenesis at the onset of human cardiac valve development. Development *140*, 2345–2353.

Wan, C.R., Chung, S., and Kamm, R.D. (2011). Differentiation of embryonic stem cells into cardiomyocytes in a compliant microfluidic system. Ann. Biomed. Eng. *39*, 1840–1847.

Wang, Y., Wu, Z., Liu, X., and Fu, Q. (2013). Gastrodin ameliorates Parkinson's disease by downregulating connexin 43. Mol. Med. Rep. *8*, 585–590.

Yang, L., Soonpaa, M.H., Adler, E.D., Roepke, T.K., Kattman, S.J., Kennedy, M., Henckaerts, E., Bonham, K., Abbott, G.W., Linden, R.M., et al. (2008). Human cardiovascular progenitor cells develop

from a KDR+ embryonic-stem-cell-derived population. Nature *453*, 524–528.

Yang, X., Pabon, L., and Murry, C.E. (2014). Engineering adolescence: maturation of human pluripotent stem cell-derived cardiomyocytes. Circ. Res. *114*, 511–523.

Zhang, J., Klos, M., Wilson, G.F., Herman, A.M., Lian, X., Raval, K.K., Barron, M.R., Hou, L., Soerens, A.G., Yu, J., et al. (2012). Extracellular matrix promotes highly efficient cardiac differentiation of human pluripotent stem cells: the matrix sandwich method. Circ. Res. *111*, 1125–1136.

Zhu, R., Blazeski, A., Poon, E., Costa, K.D., Tung, L., and Boheler, K.R. (2014). Physical developmental cues for the maturation of human pluripotent stem cell-derived cardiomyocytes. Stem Cell Res. Ther. *5*, 117.